

Oxygen-tuned Aluminum-based Halide Solid Electrolytes Enabling Low-voltage Anode Compatibility in All-Solid-State Batteries

*Wonju Kim¹, Sangwook Han¹, Sunyoung Lee¹, Jaekyun yoo¹, Chanwoong Park¹, Seungju Yu¹, Daero Won¹, Eungyeong Lee¹, Kun-hee Ko¹, Joohyeon Noh¹, Geunji Choi¹, Mireu Kim¹, and Kisuk Kang^{1, 3, 4, 5}**

¹Department of Materials Science and Engineering, Seoul National University, 1 Gwanak-ro, Gwanak-gu, Seoul, 08826, Republic of Korea

²Department of Chemistry, Seoul National University, 1 Gwanak-ro, Gwanak-gu, Seoul, 08826, Republic of Korea

³Institute of Engineering Research, College of Engineering, Seoul National University, 1 Gwanak-ro, Gwanak-gu, Seoul, 08826, Republic of Korea

⁴Center for Nanoparticle Research, Institute of Basic Science, Seoul National University, 1 Gwanak-ro, Gwanak-gu, Seoul, 08826, Republic of Korea

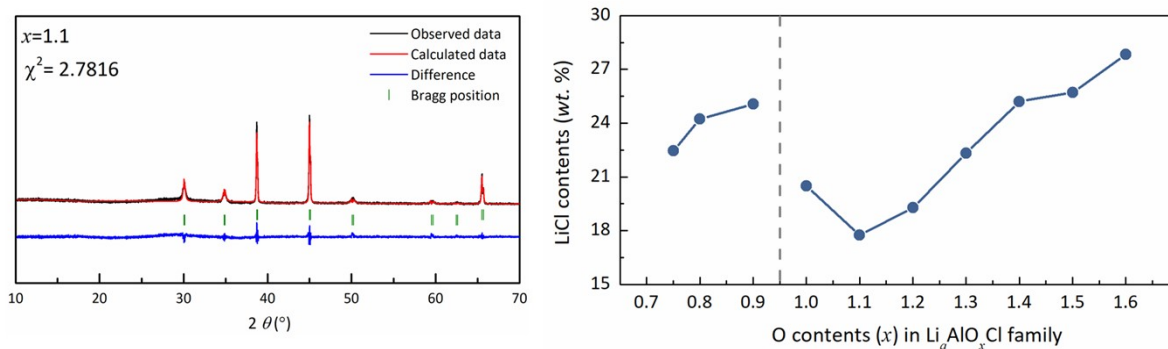
⁵Institute for Rechargeable Battery Innovations, Research Institute of Advanced Materials, Seoul National University, 1 Gwanak-ro, Gwanak-gu, Seoul 08826, Republic of Korea

*Corresponding author: K. Kang matlgen1@snu.ac.kr

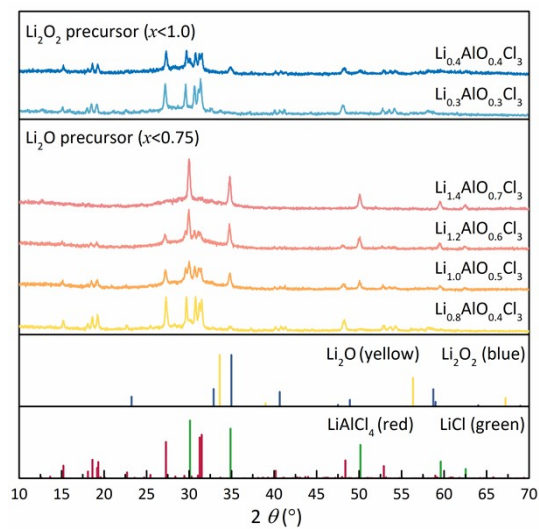
Supplementary Figures and Tables



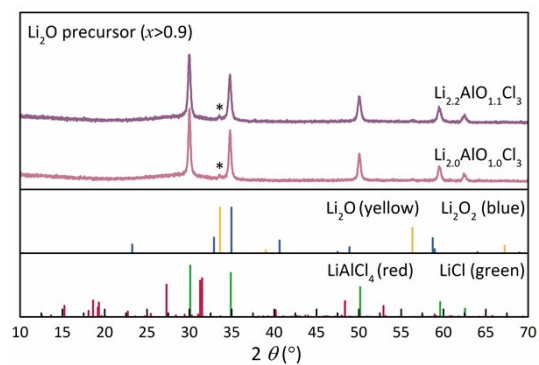
Supplementary Figure 1. Photograph of vials containing Li-Al-O-Cl solid electrolytes ($0.75 \leq x \leq 1.4$). All samples exhibit a powder-like morphology, indicating the absence of viscoelastic behavior.



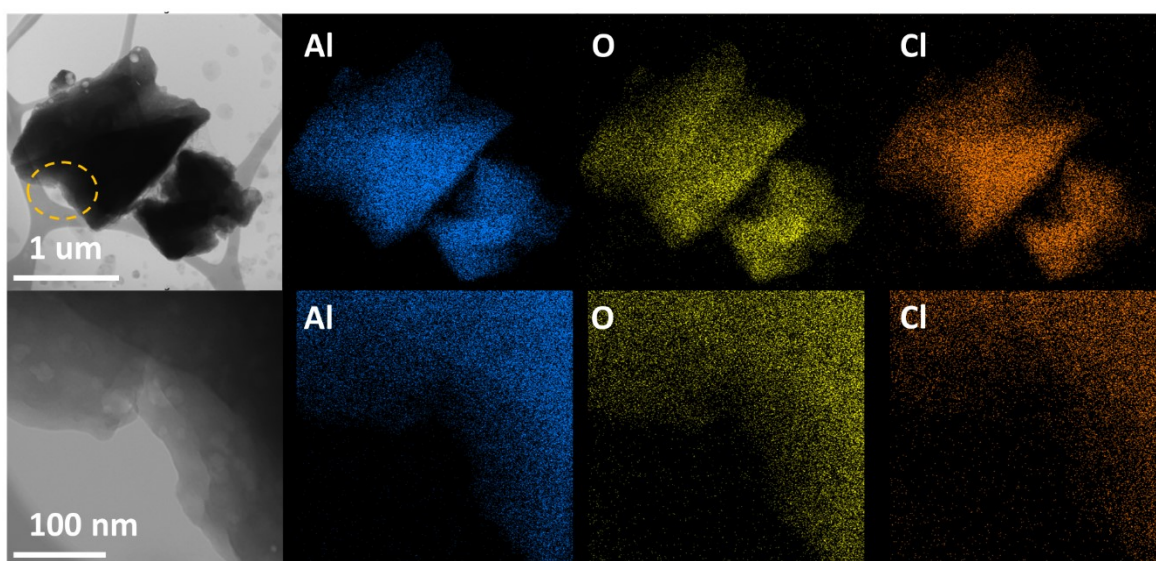
Supplementary Figure 2. LiCl contents (wt. %) calculation using Rietveld method with an internal standard^{1,2}. LiF was selected for the internal standard. The mixture of the Li-Al-O-Cl family and LiF in the weight ratio 1:1 was prepared by mixing in the agate mortar. The calculated LiCl contents (wt. %) of each Li-Al-O-Cl family via this method is displayed in the right panel. The dashed line indicates the change of O-containing precursors.



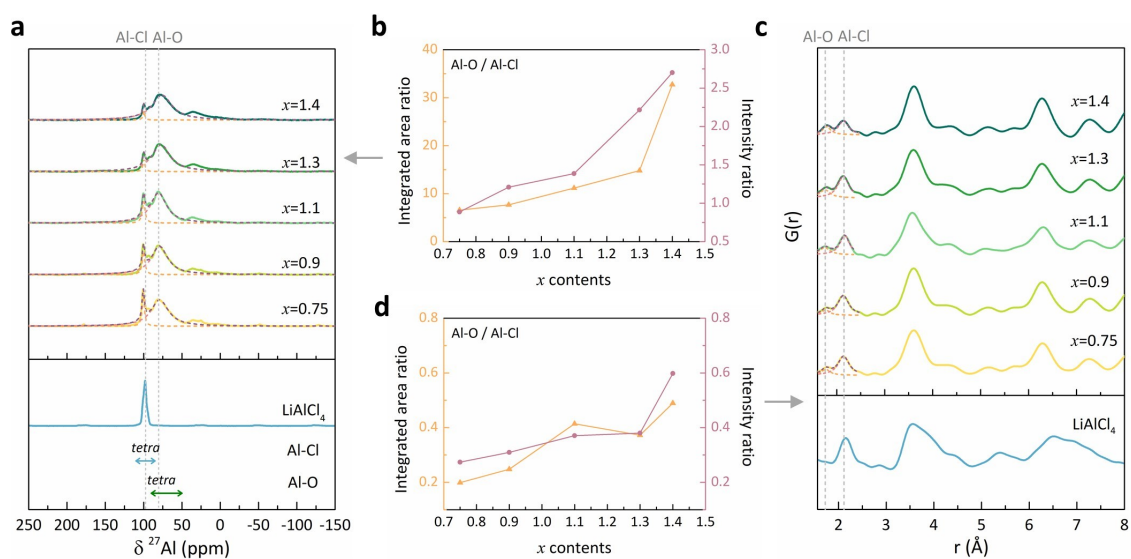
Supplementary Figure 3. XRD of $\text{Li}_a\text{AlO}_x\text{Cl}_3$ ($a = 2x, x < 0.75$; $a = x, x < 1.0$), when oxygen-containing precursor is too low. LiAlCl_4 is detected in the final product with the small signal of LiCl .



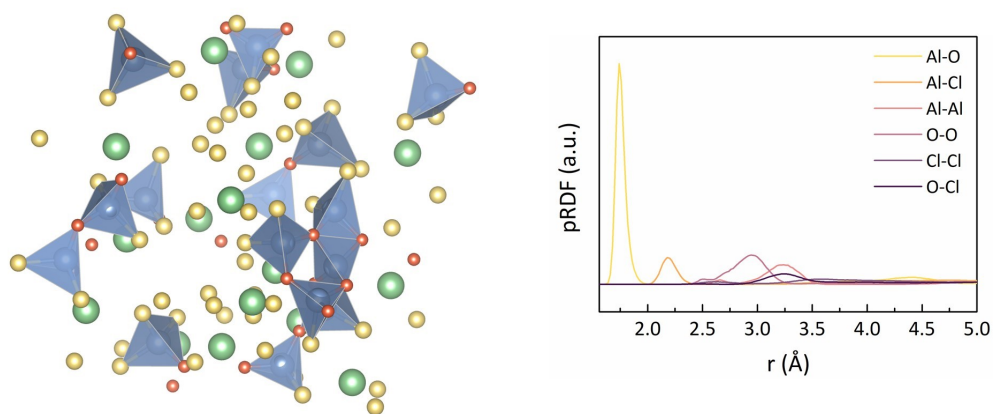
Supplementary Figure 4. XRD of $\text{Li}_a\text{AlO}_x\text{Cl}_3$ ($a = 2x, x > 0.9$). Li_2O , the oxygen containing precursor, does not fully react during the synthesis. The asterisk(*) indicates the small trace of Li_2O .



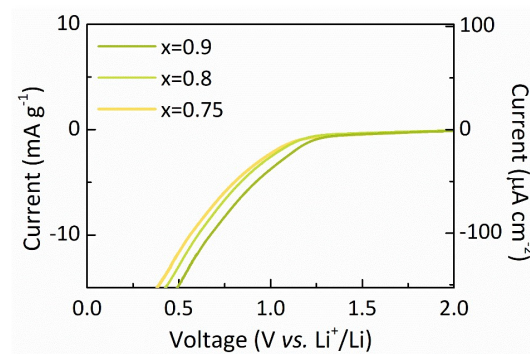
Supplementary Figure 5. EDS elemental mapping image of $x = 1.1$. The top panels are the SEM image of $x = 1.1$ and its overall EDS image (Al, O, Cl). The bottom panels are the magnified image of the dashed yellow area of $x = 1.1$ and its following EDS images. The homogeneous element distribution is observed.



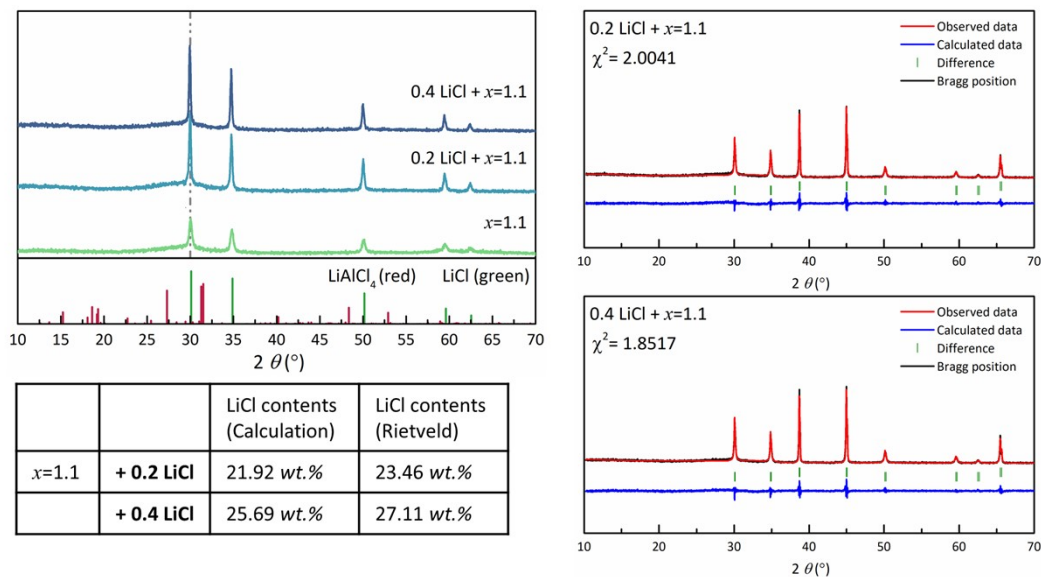
Supplementary Figure 6. a, c. Deconvoluted (a) ^{27}Al NMR spectra and (c) PDF data of Li-Al-O-Cl family ($\text{Li}_x\text{AlO}_x\text{Cl}_3$) with varying oxygen content (x). Dotted lines indicate the fitted peaks including peak indicating Al-Cl bond and Al-O bond. **b, d.** The ratios of Al-O/Al-Cl calculated from the deconvolution result of (b) ^{27}Al NMR spectra and (d) PDF data. The ratios are derived from both integrated peak areas (orange line, left y -axis) and intensities (pink line, right y -axis), all of which show systematic increases with increasing O contents (x).



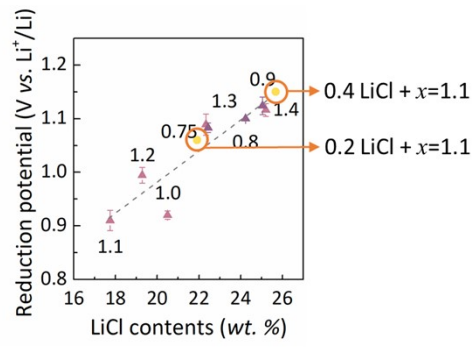
Supplementary Figure 7. The structure of LiAlOCl_3 ($x = 1$) obtained by AIMD, melt-quench method. Yellow, blue, red, and green spheres indicates Li, Al, O, and Cl, respectively. The pRDFs displayed on the right are derived from the AIMD-generated structure, which shows the great accordance with PDF results in Figure 1e.



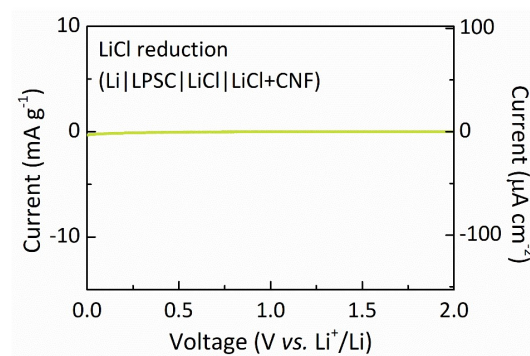
Supplementary Figure 8. LSV curves of $x = 0.75$, $x = 0.8$, and $x = 0.9$. The slight overturn of reduction onset voltages is observed with more LiCl is involved in the SEs.



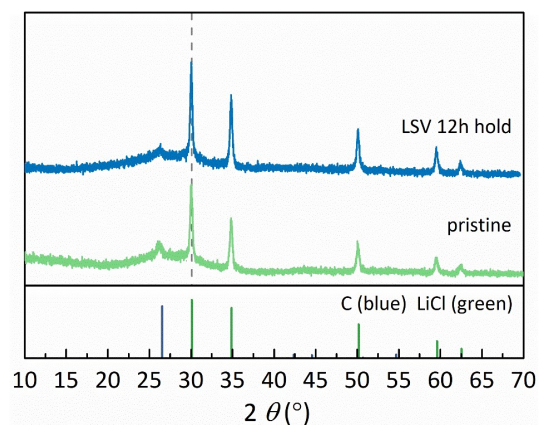
Supplementary Figure 9. XRD pattern after the additional LiCl incorporation in $x = 1.1$. The calculated LiCl contents (wt. %) using Rietveld with the internal standard (LiF)^{1, 2} and the expected LiCl contents (wt. %) display high similarities in the values. Ball-milling process in moderate conditions (300 rpm, 1 hour) was utilized to ensure the even dispersion of LiCl in the solid electrolyte, while no other structural changes at the post-treated $x = 1.1$ were detected by XRD Rietveld with the internal standard method^{1, 2}.



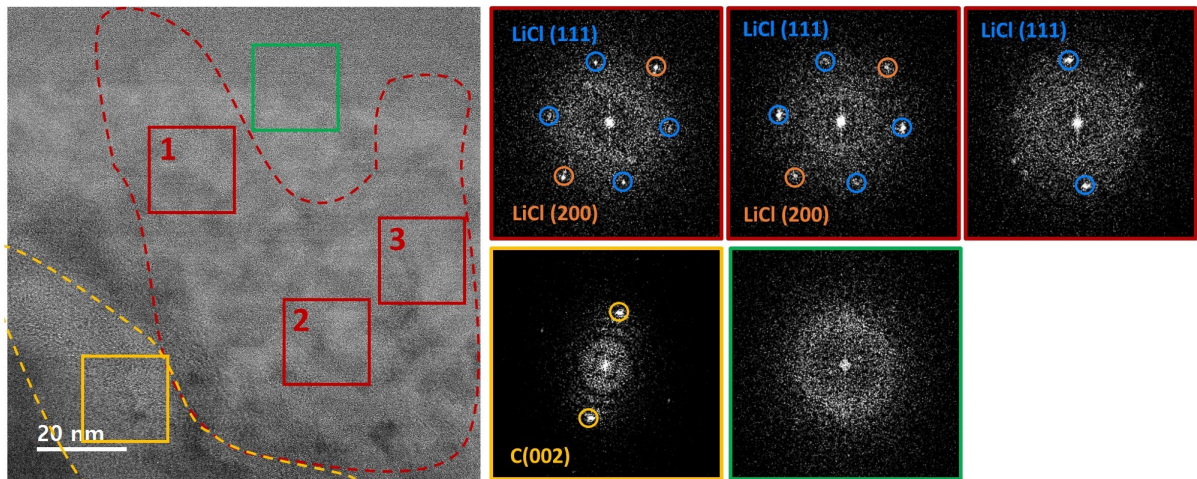
Supplementary Figure 10. Correlation between the observed reduction potential and the LiCl contents (*wt. %*). The additionally measured reduction onset potential after the LiCl addition can be analogously plotted as well.



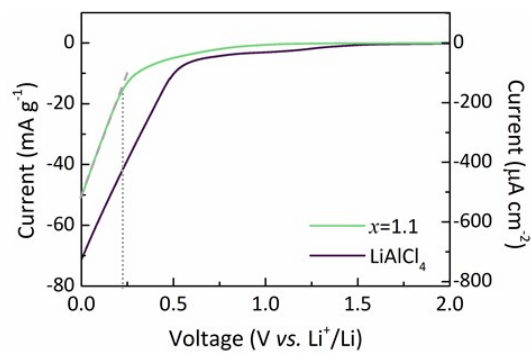
Supplementary Figure 11. LSV curve of LiCl during reduction. No significant reaction peaks are detected implying the stability of LiCl under 0 V (vs. Li⁺/Li)³.



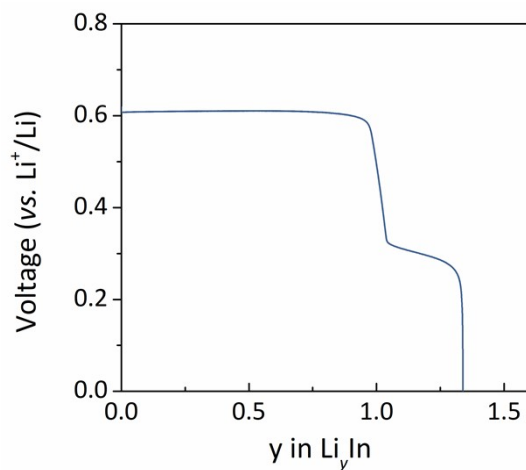
Supplementary Figure 12. XRD patterns examined before and after the LSV measurement of the $x = 1.1$ and CNF mixture (8:2 in the weight ratio). The intensity of LiCl Bragg reflection peaks is increased after the LSV. The LSV cell underwent cathodic scan till 0V and the voltage was hold at 0V for 12 hours to observe the clear change.



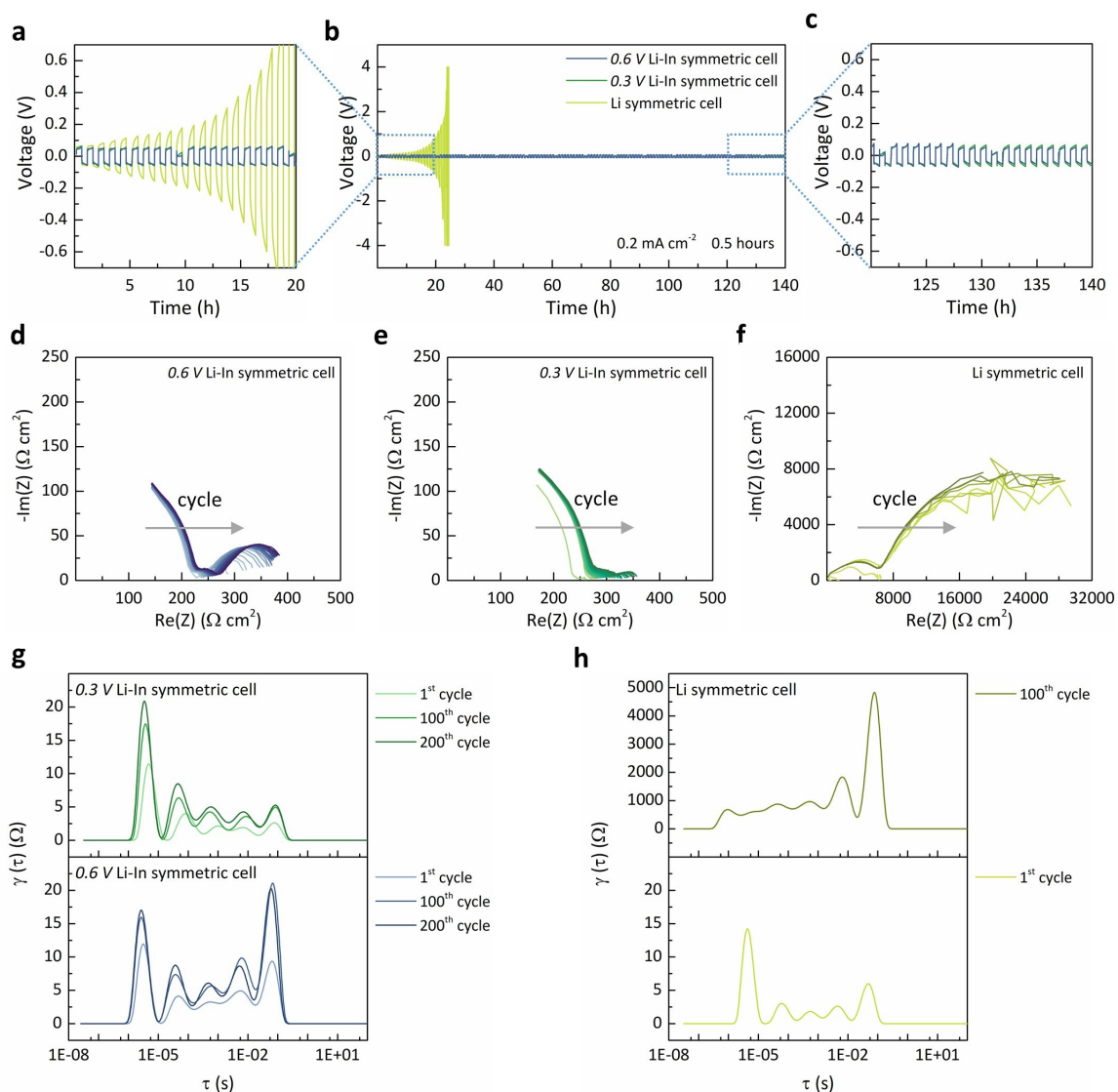
Supplementary Figure 13. TEM image and FFT patterns observed after the LSV measurement of the $x = 1.1$ and CNF mixture (8:2 in the weight ratio). The red dashed area indicates the nanocrystalline LiCl area, which is greater than the pristine $x = 1.1$ observed in Figure 1b. The corresponding FFT patterns of this red dashed area are shown on the right panels. The yellow dashed area indicates the CNF, as the corresponding FFT patterns reveals. The LSV cell underwent cathodic scan till 0V and the voltage was hold at 0 V for 12 hours to observe the clear change.



Supplementary Figure 14. LSV curves of $x = 1.1$ and LiAlCl_4 in the full scale. The current response can be divided into two distinct regions: the onset region and the linear region, where a dramatic increase in cathodic current is observed. The dashed line indicates the linear current response region for $x = 1.1$.

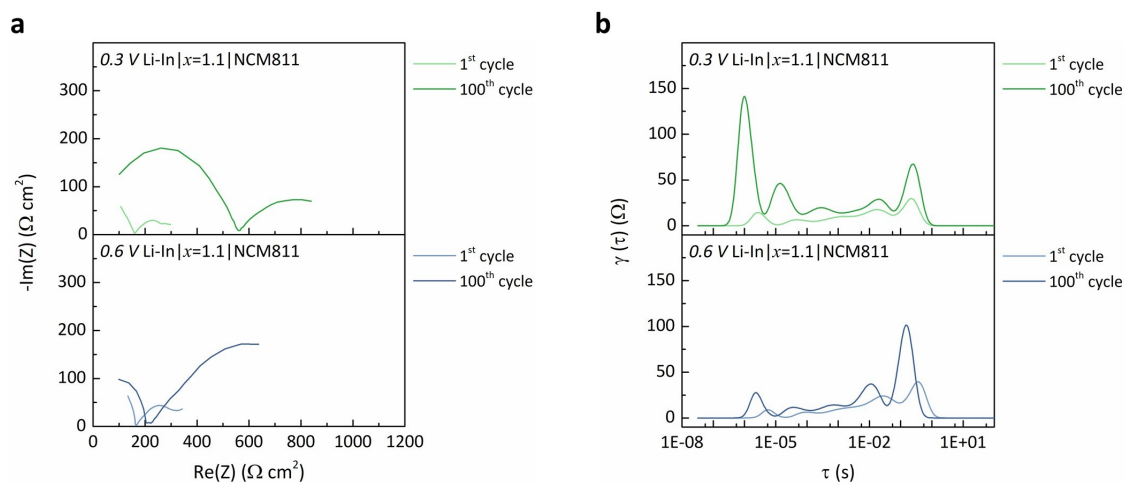


Supplementary Figure 15. Voltage profile of indium measured in a Li|LPSC|In half-cell, plotted as a function of lithium content (Li_yIn , $0 < y < 1.25$). A voltage plateau at ~ 0.6 V (vs. Li^+/Li) is observed for $0 < y < 1$, corresponding to a two-phase region between In and LiIn . A subsequent plateau at ~ 0.3 V appears for $1 < y < 1.25$, attributed to a two-phase region between LiIn and $\text{Li}_{1.25}\text{In}$ during further lithiation.

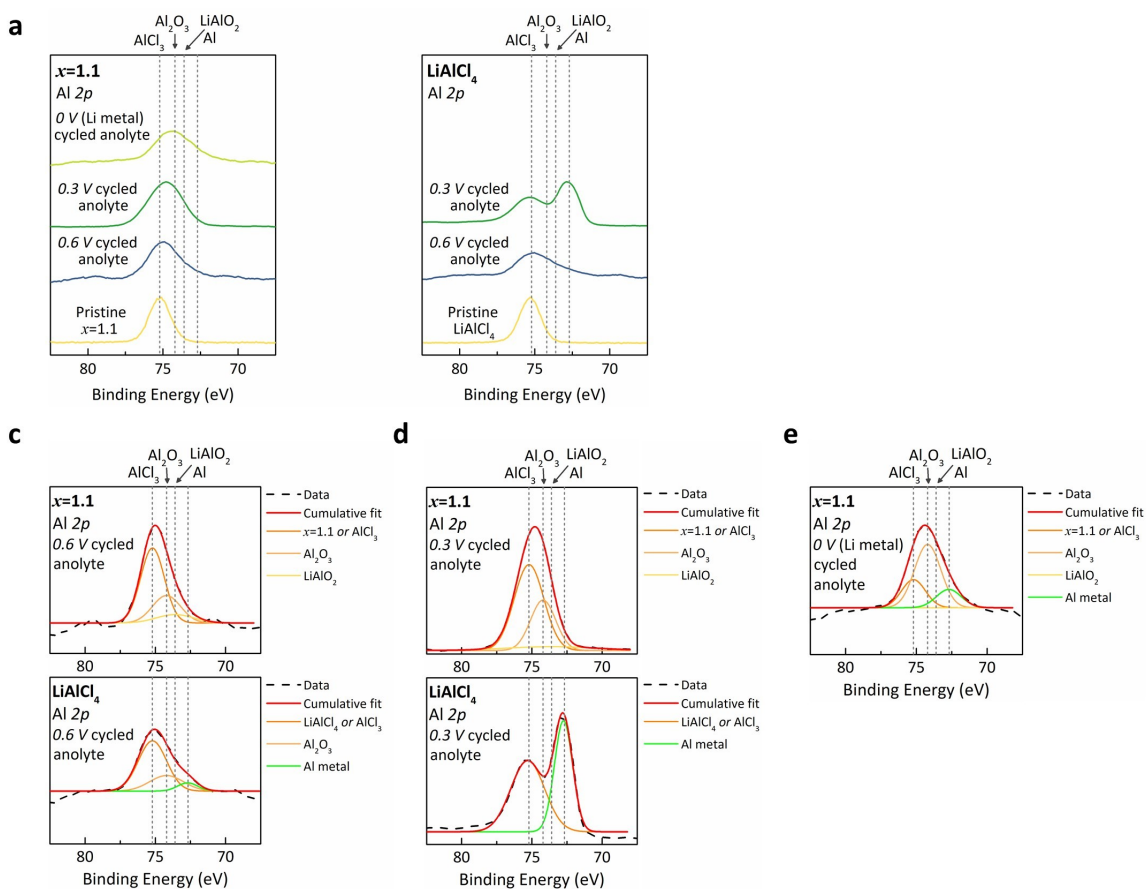


Supplementary Figure 16. **a-c.** Electrochemical performance of three symmetric cells using $0.6\text{ V Li-In}|x = 1.1|0.6\text{ V Li-In}$, $0.3\text{ V Li-In}|x = 1.1|0.3\text{ V Li-In}$, and $\text{Li}|x = 1.1|\text{Li}$ configurations. **(a)** Initial 20 hours of cycling, **(b)** extended cycling up to 140 hours, and **(c)** final 20 hours of each cell. All cells were cycled at 25°C under a current density of 0.2 mA cm^{-2} for 0.5 hours of plating/stripping intervals. **d-f.** *In situ* EIS spectra of three symmetric cells **(d)** $0.6\text{ V Li-In}|x = 1.1|0.6\text{ V Li-In}$, **(e)** $0.3\text{ V Li-In}|x = 1.1|0.3\text{ V Li-In}$, and **(f)** $\text{Li}|x = 1.1|\text{Li}$, respectively. EIS data were collected every 10 cycles during operation. **g, h.** DRT analysis of EIS spectra obtained

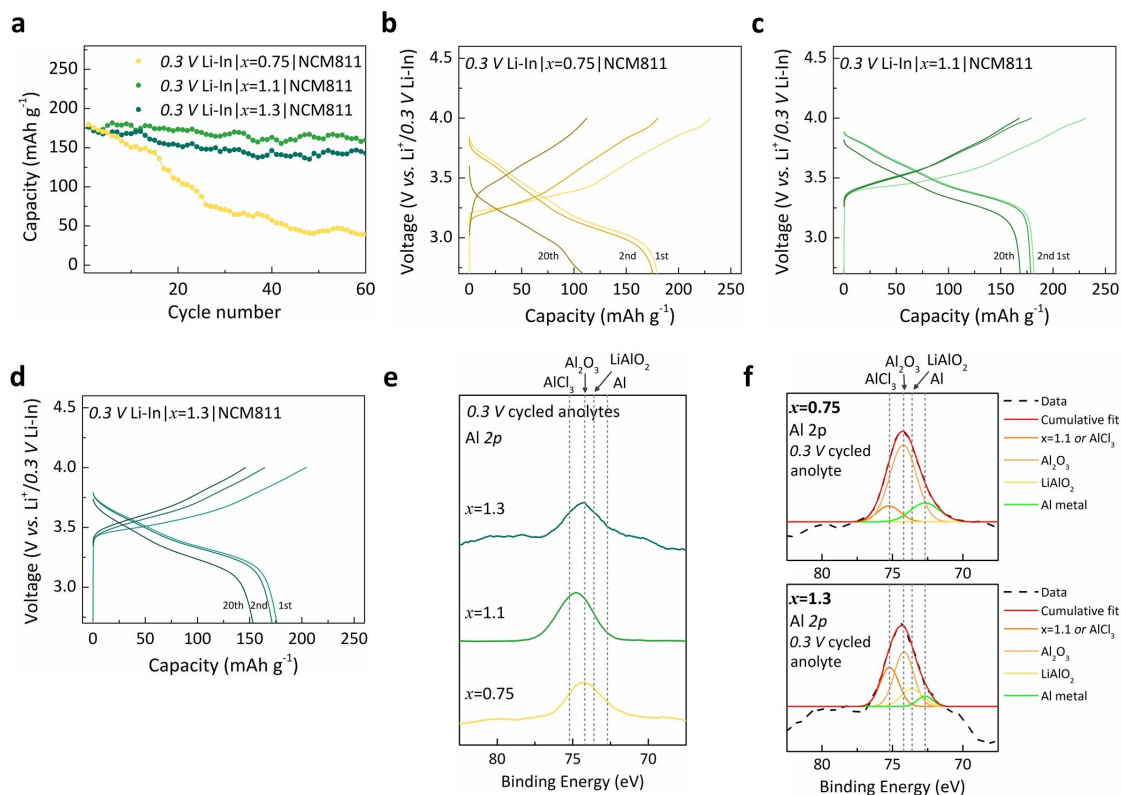
from the three symmetric cells. **(g)** DRT spectra of the 1, 100, and 200 cycles of 0.6 V Li-In (bottom panel) and 0.3 V Li-In symmetric cells (top panel). **(h)** DRT spectra of the 1 and 100 cycles of the Li symmetric cell. While the overall resistance increase of the 0.3 V and 0.6 V Li-In symmetric cell is small and comparable, the DRT analysis reveals distinct dominant components. In the 0.6 V Li-In symmetric cell, the increase is mainly observed around 10^{-2} – 10^{-1} s (charge transfer), whereas in the 0.3 V Li-In symmetric cell, the increase is more pronounced in the 10^{-7} – 10^{-5} s range (bulk-related)^{4,6}. In contrast, the Li symmetric cell exhibits increase across all relaxation time range, suggesting the absence of a stabilizing interphase and ongoing interfacial degradation.



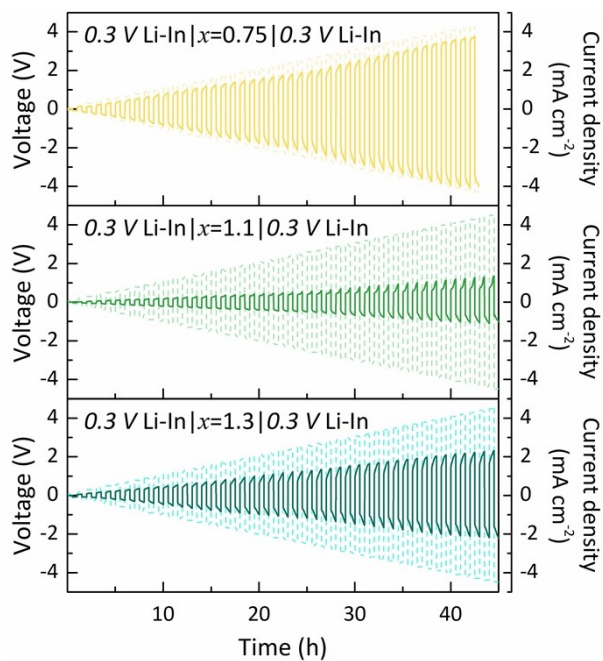
Supplementary Figure 17. a. Nyquist plots of full cells with $0.6\text{ V Li-In}|x = 1.1|\text{NCM811}$ (bottom panel) and $0.3\text{ V Li-In}|x = 1.1|\text{NCM811}$ (top panel), measured after 1 and 100 cycles. While the spectral shapes differ, the overall resistance increase remains comparable between the two cells. **b.** Corresponding DRT spectra derived from the EIS data shown in (a). In the 0.6 V Li-In cell, the increase is centered around 10^{-2} – 1 s (charge transfer), whereas in the 0.3 V Li-In cell, the increase is more pronounced in the 10^{-7} – 10^{-5} s range (bulk-related)⁴⁻⁶. These variations may reflect differences in interphase characteristics such as morphology or thickness, given that XPS results show no significant differences in chemical species of the interphase.



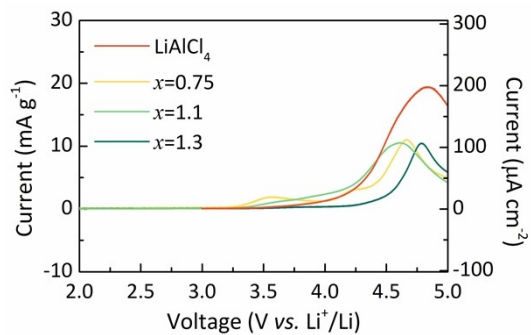
Supplementary Figure 18. a, b. Al 2p XPS spectra of pristine and cycled SEs of (a) $x = 1.1$, and (b) LiAlCl_4 . The values of 0 V, 0.3 V, and 0.6 V indicated in the graph correspond to the use of Li metal, 0.3 V Li-In, and 0.6 V Li-In as anodes, respectively. Compared to $x = 1.1$, LiAlCl_4 experiences severe decomposition when employed as the anolyte because of its poor reduction stability. **c-e.** The deconvolution of each five XPS spectra was performed to further reveal the composition of the decomposition product when cycled with (c) 0.6 V Li-In, (d) 0.3 V Li-In, and (e) Li metal (0V). LiAlCl_4 shows clear decomposition product containing Al metal regardless of the anode potential, while $x = 1.1$ decomposes into Al metal only when cycled with Li metal.



Supplementary Figure 19. a. Capacity retention of $0.3\text{ V Li-In}|x = 0.75, 1.1, \text{ or } 1.3|NCM811$ full cells. **b-d.** Charge-discharge curves for each cell with different solid electrolytes, **(b)** $x = 0.75$, **(c)** $x = 1.1$, and **(d)** $x = 1.3$. All cells were cycled at 25°C with 0.1 C in the operating voltage window $3.0\text{--}4.3\text{ V}$ (vs. Li^+/Li). **e.** Al $2p$ XPS spectra observed at the anode interphase of $0.3\text{ V Li-In}|x = 0.75, 1.1, \text{ or } 1.3|NCM811$ full cell. **f.** The deconvolution of XPS spectra was performed to reveal the composition of the decomposition product when cycled using $x = 0.75$ (top panel) and $x = 1.3$ (bottom panel).

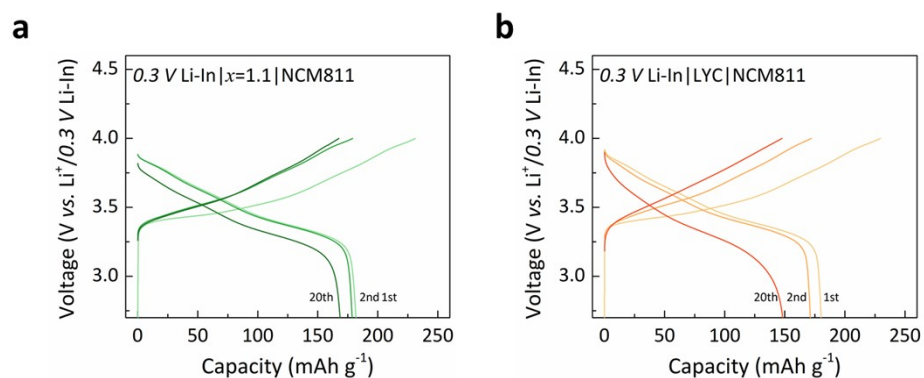


Supplementary Figure 20. CCD profiles of 0.3 V Li-In symmetric cells employing three different Li-Al-O-Cl electrolytes, with the top, middle, and bottom panels corresponding to $x = 0.75, 1.1,$ and $1.3,$ respectively. The cells were cycled at 25°C with stepwise increases in current density from 0.1 to 4.5 mA cm^{-2} . Solid lines represent the voltage response, while dotted lines indicate the applied current density.

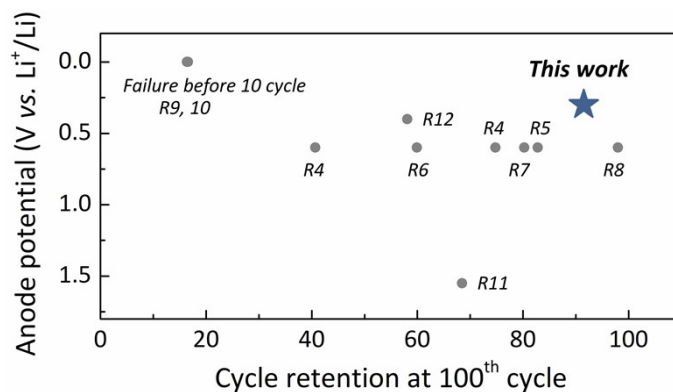


Supplementary Figure 21. LSV curves depicting oxidation behavior of LiAlCl₄, $x = 0.75$, $x = 1.1$, and $x = 1.3$. Despite oxygen incorporation, the overall composition remains chloride-rich, resulting in the oxidation stability similar to the typical chloride-based solid electrolytes⁴

11.



Supplementary Figure 22. Comparison of electrochemical performance of $x = 1.1$ and LYC. **a, b.** Charge-discharge curves of full cells with 0.3 V Li-In anode and coating-free NCM811 cathode show that **(a)** $x = 1.1$ offers superior performance with much lower overpotential than **(b)** LYC. All cells were cycled at 25°C with 0.1 C in the operating voltage window $3.0\text{--}4.3\text{ V}$ (vs. Li^+/Li).



Supplementary Figure 23. The figure illustrates the comparison of the anode potential (vs. Li⁺/Li) utilized for each solid-state cell and its cycle stability over 100 cycles. All data points represent cells fabricated using a *single* type of solid electrolyte *without* any additional secondary electrolyte^{8, 9, 11, 12, 15-19}. Unstable cells that experienced early failure are also marked in the graph. For cells that did not complete 100 cycles, the capacity retention at the final recorded cycle is shown. Our cell is highlighted with a star.

References

1. K. Yasukawa, Y. Terashi and A. Nakayama, *J. Am. Ceram. Soc.*, 1998, **81**, 2978-2982.
2. S. Zhang, F. Zhao, L.-Y. Chang, Y.-C. Chuang, Z. Zhang, Y. Zhu, X. Hao, J. Fu, J. Chen, J. Luo, M. Li, Y. Gao, Y. Huang, T.-K. Sham, M. D. Gu, Y. Zhang, G. King and X. Sun, *Journal of the American Chemical Society*, 2024, **146**, 2977-2985.
3. Y. Zhu, X. He and Y. Mo, *ACS Appl. Mater. Interfaces*, 2015, **7**, 23685-23693.
4. P. Lu, S. Gong, C. Wang, Z. Yu, Y. Huang, T. Ma, J. Lian, Z. Jiang, L. Chen, H. Li and F. Wu, *ACS Nano*, 2024, **18**, 7334-7345.
5. S.-K. Jung, H. Gwon, G. Yoon, L. J. Miara, V. Lacivita and J.-S. Kim, *ACS Energy Letters*, 2021, **6**, 2006-2015.
6. M. Hahn, D. Rosenbach, A. Krimalowski, T. Nazarenius, R. Moos, M. Thelakkat and M. A. Danzer, *Electrochimica Acta*, 2020, **344**, 136060.
7. C. Wang, J. Liang, J. Luo, J. Liu, X. Li, F. Zhao, R. Li, H. Huang, S. Zhao, L. Zhang, J. Wang and X. Sun, *Sci. Adv.*, **7**, eabh1896.
8. X. Li, J. Liang, J. Luo, M. Norouzi Banis, C. Wang, W. Li, S. Deng, C. Yu, F. Zhao, Y. Hu, T.-K. Sham, L. Zhang, S. Zhao, S. Lu, H. Huang, R. Li, K. R. Adair and X. Sun, *Energy Environ. Sci.*, 2019, **12**, 2665-2671.
9. J. Liang, X. Li, S. Wang, K. R. Adair, W. Li, Y. Zhao, C. Wang, Y. Hu, L. Zhang, S. Zhao, S. Lu, H. Huang, R. Li, Y. Mo and X. Sun, *J. Am. Chem. Soc.*, 2020, **142**, 7012-7022.
10. L. Zhou, C. Y. Kwok, A. Shyamsunder, Q. Zhang, X. Wu and L. F. Nazar, *Energy Environ. Sci.*, 2020, **13**, 2056-2063.
11. H. Kwak, D. Han, J. Lyoo, J. Park, S. H. Jung, Y. Han, G. Kwon, H. Kim, S. T. Hong, K. W. Nam and Y. S. Jung, *Adv. Energy Mater.*, 2021, **11**.
12. J. Liang, E. Maas, J. Luo, X. Li, N. Chen, K. R. Adair, W. Li, J. Li, Y. Hu, J. Liu, L. Zhang, S. Zhao, S. Lu, J. Wang, H. Huang, W. Zhao, S. Parnell, R. I. Smith, S. Ganapathy, M. Wagemaker and X. Sun, *Adv. Energy Mater.*, 2022, **12**.
13. F. Li, X. Cheng, G. Lu, Y.-C. Yin, Y.-C. Wu, R. Pan, J.-D. Luo, F. Huang, L.-Z. Feng, L.-L. Lu, T. Ma, L. Zheng, S. Jiao, R. Cao, Z.-P. Liu, H. Zhou, X. Tao, C. Shang and H.-B. Yao, *Journal of the American Chemical Society*, 2023, **145**, 27774-27787.
14. S. Wang, Q. Bai, A. M. Nolan, Y. Liu, S. Gong, Q. Sun and Y. Mo, *Angew. Chem. Int. Ed.*, 2019, **58**, 8039-8043.
15. T. Asano, A. Sakai, S. Ouchi, M. Sakaida, A. Miyazaki and S. Hasegawa, *Adv Mater*, 2018, **30**, e1803075.
16. H. Zhang, Z. Yu, J. Cheng, H. Chen, X. Huang and B. Tian, *Chinese Chemical Letters*, 2023, **34**, 108228.
17. W. Ji, D. Zheng, X. Zhang, T. Ding and D. Qu, *Journal of Materials Chemistry A*, 2021, **9**,

15012-15018.

18. T. Yoshinari, R. Koerver, P. Hofmann, Y. Uchimoto, W. G. Zeier and J. Janek, *ACS Applied Materials & Interfaces*, 2019, **11**, 23244-23253.
19. H. Huo, M. Jiang, Y. Bai, S. Ahmed, K. Volz, H. Hartmann, A. Henss, C. V. Singh, D. Raabe and J. Janek, *Nature Materials*, 2024, **23**, 543-551.